Available online at www.sciencedirect.com
SCIENCE DIRECT®
International Journal of Solids and Structures 43 (2006) 3596–3612
INTERNATIONAL JOURNAL OF SOLIDS and STRUCTURES
www.elsevier.com/locate/ijsolstr

Constitutive and damage model for 63Sn37Pb solder under uniaxial and torsional cyclic loading

Gang Chen, Xu Chen *

School of Chemical Engineering and Technology, Tianjin University, Tianjin 300072, PR China

Received 3 March 2005; received in revised form 26 September 2005
Available online 16 November 2005

Abstract

A constitutive model with Ohno–Wang kinematic hardening rule is developed and employed to simulate the isothermal cyclic behavior of Sn–Pb solder under uniaxial and torsional loading. An implicit constitutive integration scheme is presented for inelastic flow of solder. Then a modified low cycle fatigue life prediction model is put forward in which the sum of maximum shear strain range and normal strain range based on the critical plane concept is adopted to replace the uniaxial strain range used by Stolkarts et al. [Stolkarts, V., Keer, L.M., Fine, M.E., 1999. Damage evolution governed by microcrack nucleation with application to the fatigue of 63Sn–37Pb solder. J. Mech. Phys. Solids 47, 2451–2468]. Comparison of the experimental results and simulation verifies that the stress strain hysteresis loops and peak stress decline curve of solder can be reasonably modeled over a wide range of loading conditions with implement of damage coupled constitutive model, and the lifetime estimations of 63Sn37Pb solder based on the assumption of microcrack nucleation governed damage is effective to provide a conservative prediction.

Keywords: 63Sn–37Pb solder; Constitutive model; Fatigue damage; Critical plane; Cyclic plasticity

1. Introduction

Eutectic Sn–Pb solder has been widely used as a soft soldering material for mechanical connections as well as to provide electrical and thermal conduction because of its low melting point, good working performance, good wet ability, good bonding strength and low cost (Vaynman et al., 1990; Smith and Kubalak, 1979; Basaran and Chandaroy, 1998). Due to the CTE mismatch of packaging assembly, thermal stress induced by the mismatch of solder and substrate will cause the failure of solder, and eventually drive the whole assembly to fail. Good prediction of fatigue life of solder joint is desired, since the effect of fatigue analysis help to improve the package reliability and optimize design of product (Darveaux, 2002).

The deformation of solder is highly temperature and rate dependent, and there has already been a great deal of experimental and theoretical effort applied to describe the constitutive relationship of tin–lead solders (Chen

* Corresponding author. Tel.: +86 22 2740 8399; fax: +86 22 8789 3037.
E-mail address: xchen@tju.edu.cn (X. Chen).

0020-7683/$ - see front matter © 2005 Elsevier Ltd. All rights reserved.
doi:10.1016/j.ijsolstr.2005.09.010

Nomenclature

$\Delta\varepsilon$	axial total strain
$\Delta\varepsilon_{\mathrm{n}}$	normal strain range on maximum shear critical plane
$\Delta\varepsilon_{\mathrm{eq}}$	equivalent strain range
$\Delta\gamma$	shear strain range
$\Delta\gamma^{\mathrm{cycle}}$	average shear strain range at a slip plane
$\Delta\gamma_{\max}$	maximum shear strain range
$\Delta\sigma_{\mathrm{eq}}$	equivalent stress range
$\boldsymbol{\alpha}$	deviatoric backstress tensor
$\boldsymbol{\alpha}^{(i)}$	component of the deviatoric back stress
$\overline{\boldsymbol{\alpha}}^{(i)}$	magnitude of $\boldsymbol{\alpha}^{(i)}$
$\boldsymbol{\varepsilon}$	total strain tensor
$\boldsymbol{\varepsilon}^{\mathrm{e}}$	elastic strain tensor
$\boldsymbol{\varepsilon}^{\mathrm{p}}$	plastic strain tensor
$\bar{\mu}$	effective shear modulus
v	Poisson's ratio
$\bar{v}$	effective Poisson's ratio
λ	plastic multiplier
λ_1	non-dimensional specimen length
$\boldsymbol{\sigma}$	stress tensor
$\bar{\sigma}$	effective axial stress
σ_{y}	size of yield surface
$\boldsymbol{\sigma}^{\mathrm{trial}}$	trial stress tensor
$\bar{\tau}$	effective shear stress
ω	microcrack density
$\bar{\omega}_{\mathrm{c}}$	critical microcrack density
D	damage variable
D'	damage value at the end of transient stage
$\mathbf{D}^{\mathrm{e}}$	isotropic elastic stiffness tensor
E	Young's modulus for elasticity
$\overline{E}$	effective elastic modulus
F	yield surface function
G	shear modulus
$\boldsymbol{I}$	unit tensor
$\mathbf{N}$	unit normal to the yield surface at current stress point
N	number of cycles
N_{f}	number of cycles to failure
p	accumulated plastic strain
$\boldsymbol{s}$	deviatoric stress
$\mathbf{s}^{\mathrm{trial}}$	trial deviatoric stress tensor
S_{ijkl}	elastic compliance tensor of undamaged material
S^*_{ijkl}	microcrack compliance tensor
T	torque
T_{m}	melting point temperature
$h^{(i)}, r^{(i)}, \zeta^{(i)}, \eta, \chi, k, a, b, S$	material constants

et al., 2005). However, the investigation on stress strain response of solder under loading conditions other than uniaxial loading appears to be very rare. Low et al. (1991) presented that multiaxial yielding behavior of

63Sn–37Pb solder alloy more closely followed the von Mises theory for plastic deformation, and shear modulus exhibits little or no dependence on strain rate. Isothermal torsional creep tests were conducted by Schroeder and Mitchell (1992) on thin-walled tubular specimens of near-eutectic 63Sn–37Pb solder using a specially constructed torsional creep frame and troptometer, but the cyclic deformation was not involved in his work. Because the tin–lead material is too soft, the thin-walled tubular specimen used for test is difficult to machine and the torsional cyclic deformation cannot be measured by contact extensometer. Since the research on stress strain response of tin–lead solder under torsional loading is lacking, it is imperative to establish an accurate constitutive model to describe the deformation behavior of solder under both uniaxial and torsional loading conditions.

As it was shown by Lemaitre and Chaboche (Chaboche, 1998a,b), the damage evolution equation could be conveniently incorporated into continuum damage mechanics, with the effective stress concept, to characterize the cyclic fatigue behavior under various loading conditions. Thus the peak stress decline curve obtained from strain controlled experiments can be described with the appropriate damage evolution law. Recently, numerous physics of failure based models have been developed for the evaluation of reliability of solder alloys under thermo-mechanical fatigue loading, such as Basaran et al. (Basaran and Chandaroy, 1998; Basaran and Yan, 1998; Tang and Basaran, 2003), Chow et al. (Wei et al., 2004; Yang et al., 2004) and Stolkarts et al. (1998). Basaran and Yan (1998) proposed that the entropy, which was a measure of disorder in a system, could be used as a damage scaling in solid mechanics. Chow et al. (Wei et al., 2004; Yang et al., 2004) presented a damage model based on the free energy equivalence principle, and the equivalent inelastic damage energy release rate corresponding to the damage variables were derived using the theory of irreversible thermodynamics. A damage surface was postulated to bound the regime of fatigue damage and inelastic damage. Stolkarts et al. (1998) proposed a damage evolution law based on a non-linear accumulation of damage, and the damage parameters were dependent on interaction between externally applied load and creep. All damage evolution equations brought forward above can be used in conjunction with solder constitutive model. However, the numerous parameters in those models restrict their applications to engineer, and many tests have to be performed for the procedure of parameter determination.

An adoption of suitable damage parameter is the subject of this paper. A model proposed by Stolkarts et al. (Stolkarts et al., 1999, 2001; Fine et al., 1999) was chosen, for it was specifically created for tin–lead solders and showed a good correlation with experiment over a wide range of loading conditions. Since the damage evolution laws were derived based on the uniaxial cyclic test due to the limitation of available data, Stolkarts et al. (1999, 2001) arbitrarily correlated average shear strain range $\Delta\gamma^{\text{cycle}}$ at a slip plane to the total strain range $\Delta\varepsilon$. For multiaxial loading, the total strain amplitude has to be replaced with an equivalent strain range. Although Lim and Lu (2001) and Chen et al. (in press-a) all found that the uniaxial and torsional fatigue lives were comparable for 63Sn–37Pb under both uniaxial and torsional tests with the same equivalent von Mises strain amplitude, the predictions of fatigue lives are out of the bound of factor 2 on the non-conservative side under multiaxial non-proportional loading conditions (Chen et al., in press-b). To consider the effect of multiaxial loading, a specific expression of shear strain and normal strain on the maximum shear strain plane was used as damage parameter, which was based on the critical plane approach and proposed by Kandil, Brown and Miller (KBM) (Kandil et al., 1982).

The goal of this paper is to propose a constitutive model with Ohno–Wang kinematic hardening rule describing the stress strain behavior of 63Sn37Pb solder under isothermal cyclic uniaxial and torsional loading, and a modified damage evolution model proposed by Stolkarts et al. is used in conjunction with Ohno–Wang constitutive model. As will be shown later, the model correlates well with experiment over a wide range of loading conditions, and the fatigue life prediction model is a good choice in a safe design practice.

2. Experiment

2.1. Material and equipment

The chemical composition of 63Sn37Pb is given in Table 1. For manufacture of the specimen, firstly the raw material was cast in round bars whose dimensions were 110 mm in length and 35 mm in diameter at operating temperature, which was 100 °C above T_m (melting point: 183 °C), then the cast was machined to the form and

Table 1
Chemical composition

Sn	Pb	Cu	Bi	Fe	As	Sb	Cd	Zn	Ag
62.84	Bal.	0.0007	0.0026	0.0003	0.0004	0.0024	0.0001	0.0003	0.0001

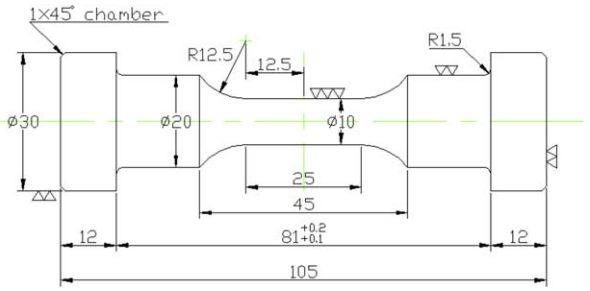

Fig. 1. Specimen geometry (unit: mm).

dimensions in Fig. 1. The geometry of the specimen was selected such that it can be used with a specially designed grip for solder materials. The specimen was fully aged at room temperature for more than 20 days.

A series of experiments was performed on an Instron axial–torsional servo-hydraulic testing machine with a digital controller. All cyclic tests were carried out under fully reversed strain control at constant strain rate of 0.5%/s. A biaxial fatigue extensometer of 15 mm in gauge length was employed to measure the axial elongation and shear deformation. Please refer to Chen et al. (in press-a) for the details of experiment.

2.2. Stress analysis

For a round solid specimen, the shear stress at the outer radius is not straightforward to be determined because of the gradient along the radius. Here, the method proposed by Miller and Chandler (1970) approach and also used in (Brown, 1978; Lin et al., 1992) can be presented as:

$$\tau = \frac{1}{2\pi R^3}\left[3T + \gamma\frac{\mathrm{d}T}{\mathrm{d}\gamma}\right] \tag{1}$$

where R is the specimen radius, T is the torque, γ is the shear strain, and $\mathrm{d}T/\mathrm{d}\gamma$ is the slope of the $T-\gamma$ hysteresis loop. Thus the shear stress on the specimen surface can be calculated directly from the torque and degree curves when the solid cylindrical specimens subjected to cyclic torsional loading. Note that Eq. (1) is valid for both elastic and plastic regimes, but the method is not feasible for non-proportional loading conditions, as pointed out by Lin et al. (1992).

In order to compare the axial and torsional behavior, an equivalent strain and stress are defined as

$$\varepsilon_{\mathrm{eq}} = \sqrt{\varepsilon^2 + \gamma^2/3}, \quad \sigma_{\mathrm{eq}} = \sqrt{\sigma^2 + 3\tau^2} \tag{2}$$

where ε and σ are axial strain and stress, respectively. γ and τ are shear strain and stress, respectively. Therefore, the stress and strain curves in following figures are plotted as

For axial direction $\varepsilon_{\mathrm{eq}} = \varepsilon$, $\sigma_{\mathrm{eq}} = \sigma$.
For torsional direction $\varepsilon_{\mathrm{eq}} = \gamma/\sqrt{3}$, $\sigma_{\mathrm{eq}} = \sqrt{3}\tau$.

2.3. Axial and torsional cyclic behavior

To understand the characteristic of low cycle fatigue of tin–lead solder, a series of tests with constant strain amplitude were carried out and listed in Table 2 under uniaixal and torsional loading. It was assumed that the

Table 2
The experimental results of 63Sn37Pb under uniaxial and torsional loading

Case	Load	$\Delta\varepsilon/2$(%)	$\Delta\gamma/2$(%)	Fatigue life
Sn-23	Axial	0.2	/	13373
Sn-33	Axial	0.3	/	8187
Sn-18	Axial	0.5	/	2521
Sn-34	Axial	0.7	/	1432
Sn-20	Torsional	/	0.346	12962
Sn-07	Torsional	/	0.692	4974
Sn-30	Torsional	/	0.866	2388
Sn-38	Torsional	/	1.819	398
Sn-31	Torsional	/	2.598	250
Sn-02	Torsional	/	3.464	120

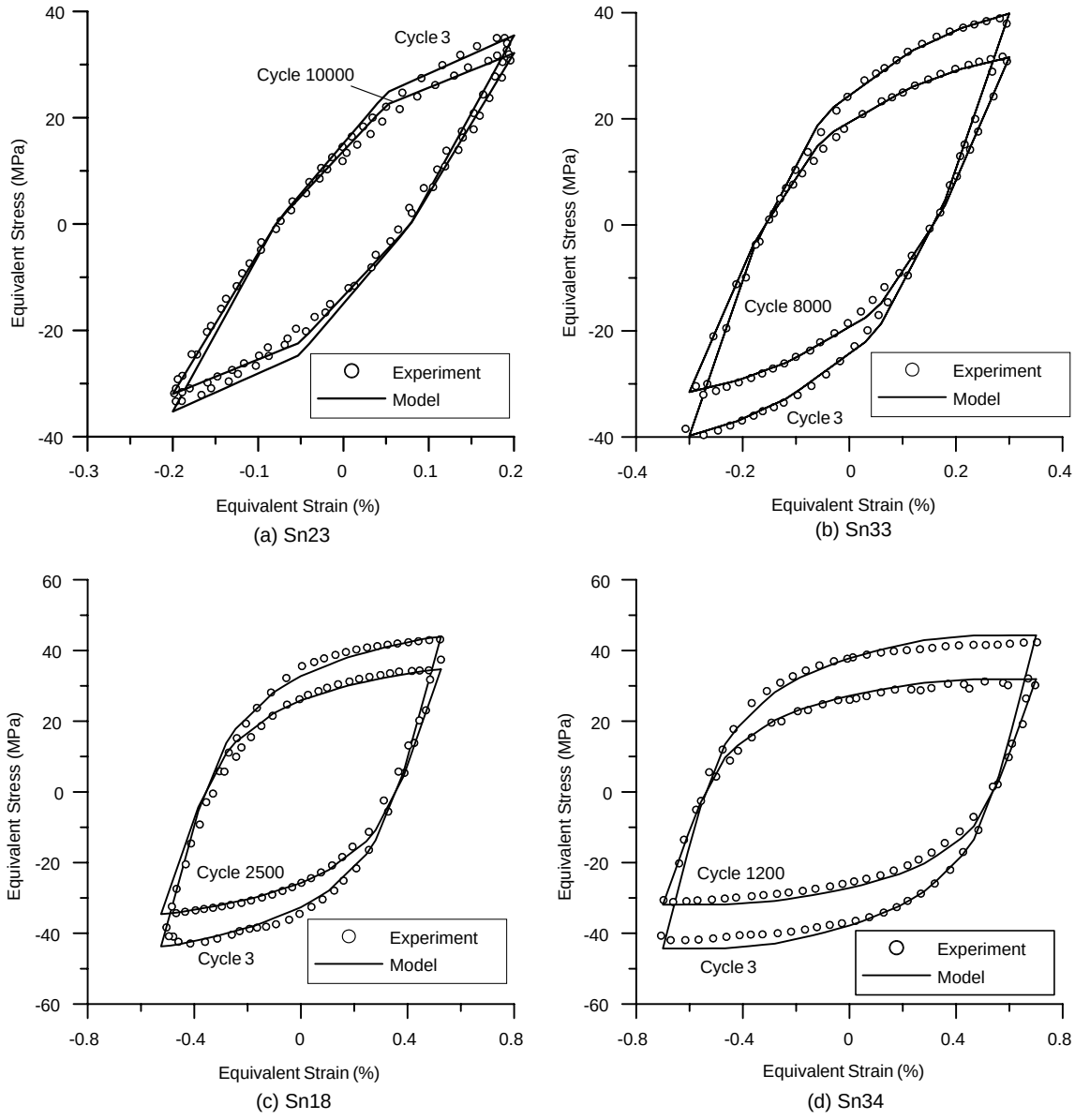

Fig. 2. Equivalent stress strain loop with damage under axial loading.

third cycle represents the damage-free material behavior and has reached cyclically stable deformation, though the stress never become stable during fatigue test. The stress strain responses corresponding to the third cycle for uniaxial and torsional loading are plotted in Figs. 2 and 3, respectively. The variations of stress amplitude with the number of cycles are given in Fig. 4 for several strain amplitudes under uniaxial and torsional fatigue loading. Stress drop mainly due to the damage evolution governed by nucleation of microcracks occurs, when a transition from one dominated by microcrack nucleation to one dominated by macrocrack dominated, the specimen can be determined as failure (Stolkarts et al., 1999). The descending curve of peak stress with cycle can be divided into three stages: transient, steady state and tertiary. The first stage is the shortest and characterized by an initial sharp drop in peak stress. The second stage has the longest duration and takes almost a constant rate of decline. Finally, the third stage shows an accelerated decline in peak stress leading to ultimate failure. It seems the transient and tertiary region is rather short compared to the steady state, and damage evolution during steady state fatigue is the emphasis for tin–lead life analysis. As it has been shown by Stolkarts et al. (1999), evolution of damage is governed by microcrack nucleation up to the turning point from the steady state to the tertiary state. The change of the slope in peak stress decline curve is used here as a failure criterion.

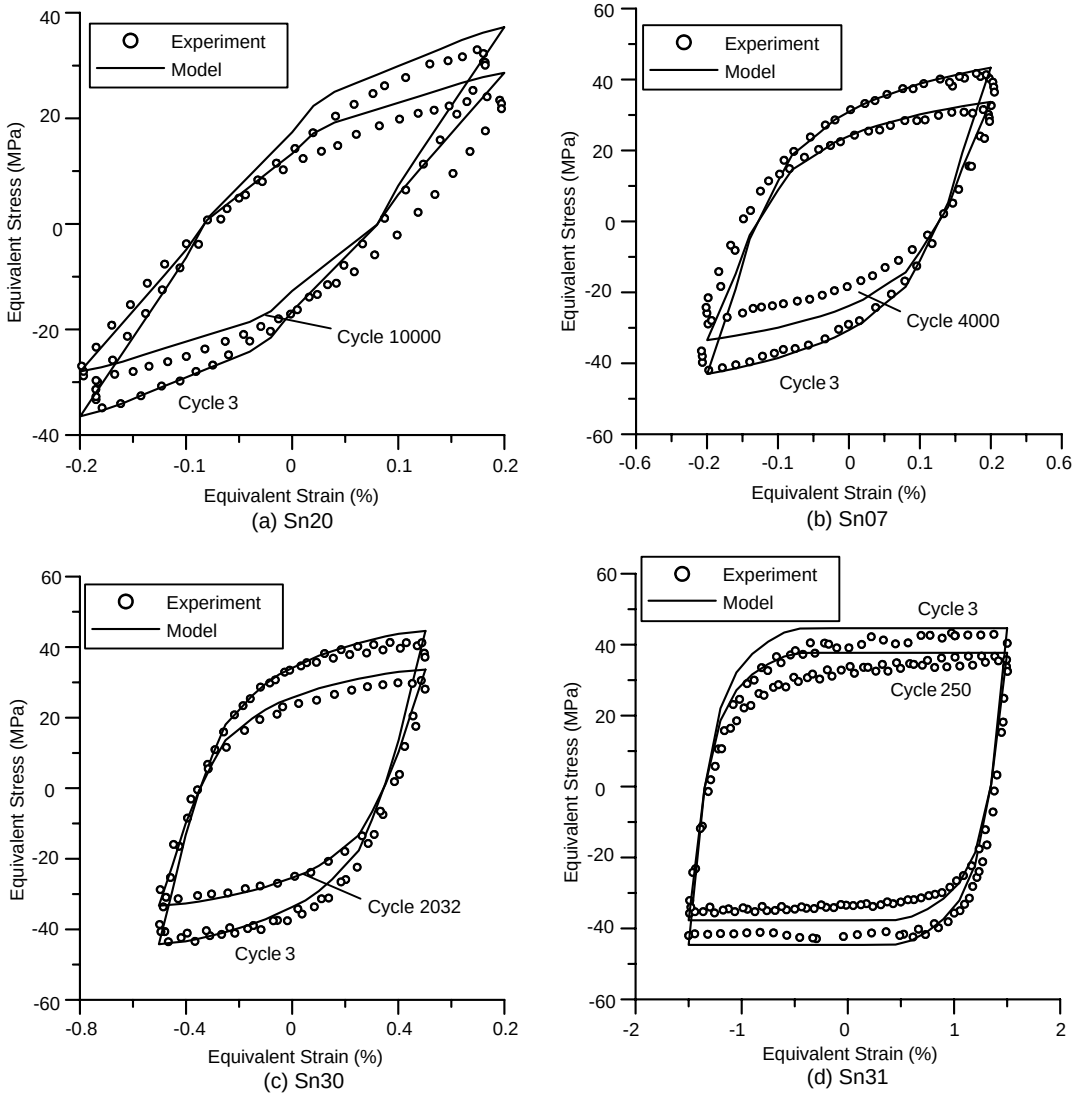

Fig. 3. Equivalent stress strain loop with damage under torsional loading.

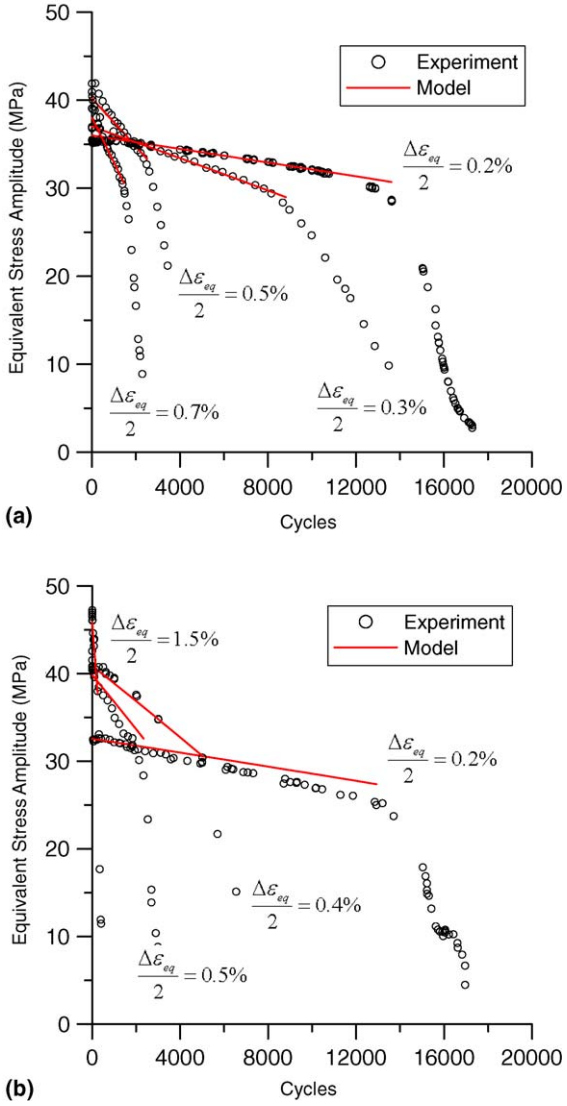

Fig. 4. Equivalent stress amplitude drop with the number of cycles. (a) Axial and (b) torsional.

This criterion is somewhat conservative since the initiation of one or several macrocracks in the material may have reached from 60 to 80 percent of its total life, but it is still a good choice in a safe design practice.

3. Constitutive model

It is assumed that the total strain is decomposed into an elastic strain part and a plastic part:

$$\boldsymbol{\varepsilon} = \boldsymbol{\varepsilon}^{\mathrm{e}} + \boldsymbol{\varepsilon}^{\mathrm{p}} \tag{3}$$

and that the elastic part obeys Hooke's law:

$$\boldsymbol{\varepsilon}^{\mathrm{e}} = \frac{1+\nu}{E}\boldsymbol{\sigma} - \frac{\nu}{E}(\mathrm{tr}\boldsymbol{\sigma})\mathbf{I} \tag{4}$$

or

$$\boldsymbol{\sigma} = \mathbf{D}^{\mathrm{e}} : \boldsymbol{\varepsilon}^{\mathrm{e}} \tag{5}$$

where $\boldsymbol{\sigma}$ denotes stress tensor, $\mathbf{I}$ is a unit tensor, $\mathbf{D}^{\mathrm{e}}$ represents isotropic elastic stiffness tensor, (:) the inner product between tensors.

The plastic flow rule can be stated as

$$\dot{\boldsymbol{\varepsilon}}^{\mathrm{p}} = \dot{\lambda}\frac{\partial F}{\partial \boldsymbol{\sigma}} \tag{6}$$

The material is assumed to follow the von Mises yield criterion, which is given by

$$F = \frac{3}{2}(\mathbf{s}-\boldsymbol{\alpha}) : (\mathbf{s}-\boldsymbol{\alpha}) - \sigma_y^2 = 0 \tag{7}$$

where λ is plastic multiplier, which can be determined using the consistency condition $\dot{F} = 0$. $\mathbf{s} = \boldsymbol{\sigma} - \frac{1}{3}\mathrm{tr}(\boldsymbol{\sigma})\mathbf{I}$ is the deviatoric stress tensor, $\boldsymbol{\alpha}$ is deviatoric back stress, and σ_{y} is the size of the yield surface. In general, plastic multiplier λ is replaced by accumulated plastic strain rate p which is expressed by

$$\dot{p} = \left(\frac{2}{3}\dot{\boldsymbol{\varepsilon}}^{\mathrm{p}} : \dot{\boldsymbol{\varepsilon}}^{\mathrm{p}}\right)^{1/2} \tag{8}$$

with the differential of yield surface from Eq. (7) and substitute it in Eq. (6), one obtains:

$$\mathbf{N} = \sqrt{\frac{3}{2}}\frac{\mathbf{s}-\boldsymbol{\alpha}}{\sigma_y} \tag{9}$$

$$\dot{\boldsymbol{\varepsilon}}^{\mathrm{p}} = \sqrt{\frac{3}{2}}\dot{p}\mathbf{N} \tag{10}$$

Replace $\mathbf{N}$ with Eq. (9),

$$\dot{\boldsymbol{\varepsilon}}^{\mathrm{p}} = \frac{3}{2}\dot{p}\frac{\mathbf{s}-\boldsymbol{\alpha}}{\sigma_y} \tag{11}$$

where $\mathbf{N}$ is unit normal to the yield surface at current stress point and denotes the plastic flow direction.

Ohno and Wang (Ohno and Wang, 1993a,b) used a multilinear model in which several kinematic hardening rules of the Armstrong–Frederic type were superposed. They assumed that each component of back stress $\boldsymbol{\alpha}^{(i)}$ had a critical state for its dynamic recovery term to be activated. The Ohno–Wang model is proposed in the following form:

$$\begin{aligned}
&\text{Model(I):} \quad \boldsymbol{\alpha} = \sum_{1}^{M}\boldsymbol{\alpha}^{(i)}, \quad \dot{\boldsymbol{\alpha}}^{(i)} = h^{(i)}\left[\frac{2}{3}\dot{\boldsymbol{\varepsilon}}^{\mathrm{p}} - H(f^{(i)})\left\langle \dot{\boldsymbol{\varepsilon}}^{\mathrm{p}} : \frac{\boldsymbol{\alpha}^{(i)}}{\overline{\boldsymbol{\alpha}}^{(i)}}\right\rangle \frac{\boldsymbol{\alpha}^{(i)}}{r^{(i)}}\right] \\
&\qquad f^{(i)} = \overline{\boldsymbol{\alpha}}^{(i)} - r^{(i)^2}
\end{aligned} \tag{12}$$

$$\text{Model(II):} \quad \boldsymbol{\alpha} = \sum_{i=1}^{M}\boldsymbol{\alpha}^{(i)}, \quad \dot{\boldsymbol{\alpha}}^{(i)} = h^{(i)}\left[\frac{2}{3}\dot{\boldsymbol{\varepsilon}}^{\mathrm{p}} - \left(\frac{\overline{\boldsymbol{\alpha}}^{(i)}}{r^{(i)}}\right)^{m^{(i)}}\left\langle \dot{\boldsymbol{\varepsilon}}^{\mathrm{p}} : \frac{\boldsymbol{\alpha}^{(i)}}{\overline{\boldsymbol{\alpha}}^{(i)}}\right\rangle \frac{\boldsymbol{\alpha}^{(i)}}{r^{(i)}}\right] \tag{13}$$

where M denotes the number of parts of back stress, $\boldsymbol{\alpha}^{(i)}$ is the ith component of the deviatoric back stress $\boldsymbol{\alpha}$, $\overline{\boldsymbol{\alpha}}^{(i)}$ is the magnitude of $\boldsymbol{\alpha}^{(i)}$, $\overline{\boldsymbol{\alpha}}^{(i)} = \sqrt{3/2\boldsymbol{\alpha}^{(i)} : \boldsymbol{\alpha}^{(i)}}$, $h^{(i)}$, $r^{(i)}$ are material constants, H stands for the Heaviside step function, $\langle\rangle$ the Macauley bracket, i.e. $\langle x\rangle = (x + |x|)/2$.

The parameters in the Ohno–Wang model used in this study are determined by the tensile curve from uniaxial loading referred to Ohno (1998), it is found that nine hardening rules are sufficient to obtain a good stable uniaxial hysteresis loop simulation for 63Sn37Pb. For materials like eutectic solder, the real yield stress is difficult to determine from experiment since the inelastic deformation will occur even if the load is very small. As it was pointed out by Jiang and Kurath (1996) that OW model is not sensitive to yield stress value and the larger plastic strain is almost irrespective to the choice of yield stress, thus the yield stress is set as 2 MPa. All the parameters are presented in Table 3.

Table 3
Parameters for Ohno–Wang's model

σ_y (MPa)	2
E (MPa)	28 000
v	0.37
$\zeta_{1-9} = 63520, 4340, 1215, 810, 500, 375, 295, 235, 171$	
$r_{1-9} = 16.7, 10.6, 3.64, 2.6, 2.47, 1.27, 3.54, 3.09, 0.21$ MPa	

4. Backward Euler method

Many explicit (Ortiz and Simo, 1986), semi-implicit (Fu et al., 1996; Marin and McDowell, 1997), and implicit (Ortiz and Popov, 1985; Simo and Taylor, 1985, 1986; Lush et al., 1989; Duxbury et al., 1994; Hartmann et al., 1997; Kobayashi and Ohno, 2002; Kobayashi et al., 2003) time integration procedures for rate-independent and rate-dependent plasticity have been proposed in the literature. Among those methods, backward Euler scheme is widely used for its high accuracy and unconditional stability properties. To solve the combination of yield equation, flow equation, hardening equation and satisfy the consistency condition at each time step, Simo and Taylor (1985, 1986) proposed an operator splitting method, which uses an elastic predictor to set an initial condition and a plastic corrector to update yield surface. With the assumption of isotropic deformation and incompressible inelasticity, backward Euler method can be implemented to implicitly integrate stress by iteratively solving a scalar equation until its convergence (Duxbury et al., 1994; Hartmann et al., 1997; Kobayashi and Ohno, 2002). In this paper, backward Euler algorithm has presented for a finite increment of loading, such that the following mechanical transformation is carried out:

$$(\boldsymbol{\sigma}_n, \boldsymbol{\alpha}_n^{(i)}, \boldsymbol{\varepsilon}_n, \boldsymbol{\varepsilon}_n^{\mathrm{p}}, p_n) \overset{\Delta\boldsymbol{\varepsilon}_{n+1}}{\longrightarrow} \left(\boldsymbol{\sigma}_{n+1}, \boldsymbol{\alpha}_{n+1}^{(i)}, \boldsymbol{\varepsilon}_{n+1}, \boldsymbol{\varepsilon}_{n+1}^{\mathrm{p}}, p_{n+1}\right) \tag{14}$$

The subscripts n and $n+1$ signify the values at n and $n+1$, respectively, and Δ denotes the increments in the interval from n to $n+1$. As shown by Stolkarts et al. (1999), there is no isotropic hardening observed in cyclic experiments of 63Sn37Pb solder. Yield stress is assumed to be constant during the whole successive iterations.

The discretized forms of Eqs. (3)–(13) are listed below:

$$\boldsymbol{\varepsilon}_{n+1} = \boldsymbol{\varepsilon}_{n+1}^{\mathrm{e}} + \boldsymbol{\varepsilon}_{n+1}^{\mathrm{p}} \tag{15}$$

$$\boldsymbol{\sigma}_{n+1} = \mathbf{D}^{\mathrm{e}} : \boldsymbol{\varepsilon}_{n+1}^{\mathrm{e}} \tag{16}$$

$$\Delta\boldsymbol{\varepsilon}_{n+1}^{\mathrm{p}} = \sqrt{\frac{3}{2}}\Delta p_{n+1}\mathbf{N}_{n+1} \tag{17}$$

$$\mathbf{N}_{n+1} = \sqrt{\frac{3}{2}}\frac{\mathbf{s}_{n+1} - \boldsymbol{\alpha}_{n+1}}{\sigma_y} \tag{18}$$

$$\Delta\boldsymbol{\varepsilon}_{n+1}^{\mathrm{p}} = \frac{3}{2}\Delta p_{n+1}\frac{\mathbf{s}_{n+1} - \boldsymbol{\alpha}_{n+1}}{\sigma_y} \tag{19}$$

$$\boldsymbol{\alpha}_{n+1} = \sum_{1}^{M} \boldsymbol{\alpha}_{n+1}^{(i)} \tag{20}$$

$$F_{n+1} = \frac{3}{2}(\mathbf{s}_{n+1} - \boldsymbol{\alpha}_{n+1}) : (\mathbf{s}_{n+1} - \boldsymbol{\alpha}_{n+1}) - \sigma_y^2 = 0 \tag{21}$$

First, a trial stress is computed by using return mapping with respect to the total strain increment $\Delta\boldsymbol{\varepsilon}_{n+1}$:

$$\boldsymbol{\sigma}_{n+1}^{\mathrm{trial}} = \boldsymbol{\sigma}_n + \mathbf{D}^{\mathrm{e}} : \Delta\boldsymbol{\varepsilon}_{n+1} = \mathbf{D}^{\mathrm{e}} : \left[(\boldsymbol{\varepsilon}_n - \boldsymbol{\varepsilon}_n^{\mathrm{p}}) + \Delta\boldsymbol{\varepsilon}_{n+1}\right] = \mathbf{D}^{\mathrm{e}} : \left[(\boldsymbol{\varepsilon}_{n+1} - \boldsymbol{\varepsilon}_{n+1}^{\mathrm{p}}) + \Delta\boldsymbol{\varepsilon}_{n+1}^{\mathrm{p}}\right] = \boldsymbol{\sigma}_{n+1} + \mathbf{D}^{\mathrm{e}} : \Delta\boldsymbol{\varepsilon}_{n+1}^{\mathrm{p}} \tag{22}$$

where $\mathbf{D}^{\mathrm{e}} : \Delta\boldsymbol{\varepsilon}_{n+1}$ and $\mathbf{D}^{\mathrm{e}} : \Delta\boldsymbol{\varepsilon}_{n+1}^{\mathrm{p}}$ is the elastic predictor and plastic corrector, respectively. With the assumption of elastic isotropy and plastic incompressibility, we have:

$$\mathbf{D}^{\mathrm{e}} : \Delta\boldsymbol{\varepsilon}_{n+1}^{\mathrm{p}} = 2G\Delta\boldsymbol{\varepsilon}_{n+1}^{\mathrm{p}} \tag{23}$$

where

$$G = \frac{E}{2(1+v)} \tag{24}$$

G represents the plastic shear modulus. Since Eq. (23) is tenable when complete plastic flow status occurs, v is assigned 0.5 in Eq. (24) to calculate G.

From Eqs. (22) and (23), and with the relation of stress tensor and deviatoric stress tensor, one has

$$\mathbf{s}_{n+1} = \mathbf{s}_{n+1}^{\text{trail}} - 2G\Delta\boldsymbol{\varepsilon}_{n+1}^{\text{p}} \tag{25}$$

To make simplicity of Ohno–Wang model, we use $\dot{p}^{(i)}$ to express the former part of dynamic recovery term, that is:

$$\text{For Model(I)}: \quad \dot{p}^{(i)} = H(f^{(i)})\left\langle \dot{\boldsymbol{\varepsilon}}^{\text{p}} : \frac{\boldsymbol{\alpha}^{(i)}}{\overline{\boldsymbol{\alpha}}^{(i)}} \right\rangle \tag{26}$$

$$\text{For Model(II)}: \quad \dot{p}^{(i)} = \left(\frac{\overline{\boldsymbol{\alpha}}^{(i)}}{r^{(i)}}\right)^{m^{(i)}} \left\langle \dot{\boldsymbol{\varepsilon}}^{\text{p}} : \frac{\boldsymbol{\alpha}^{(i)}}{\overline{\boldsymbol{\alpha}}^{(i)}} \right\rangle \tag{27}$$

Hence it gives

$$\dot{\boldsymbol{\alpha}}^{(i)} = h^{(i)}\left[\frac{2}{3}\dot{\boldsymbol{\varepsilon}}^{\text{p}} - \dot{p}^{(i)}\frac{\boldsymbol{\alpha}(i)}{r^{(i)}}\right] \tag{28}$$

If one defines $\zeta^{(i)} = \frac{h^{(i)}}{r^{(i)}}$, a unified form of Eqs. (12) and (13) can be obtained as:

$$\boldsymbol{\alpha} = \sum_{i=1}^{M} \boldsymbol{\alpha}^{(i)}, \quad \dot{\boldsymbol{\alpha}}^{(i)} = \frac{2}{3}h^{(i)}\dot{\boldsymbol{\varepsilon}}^{\text{p}} - \zeta^{(i)}\dot{p}^{(i)}\boldsymbol{\alpha}^{(i)} \tag{29}$$

The above dynamic hardening rule can be written in a discretized form:

$$\boldsymbol{\alpha}_{n+1}^{(i)} = \theta_{n+1}^{(i)}\left(\boldsymbol{\alpha}_{n}^{(i)} + \frac{2}{3}h^{(i)}\Delta\boldsymbol{\varepsilon}_{n+1}^{\text{p}}\right) \tag{30}$$

where $\theta_{n+1}^{(i)}$ is defined by the following equation and satisfies $0 < \theta_{n+1}^{(i)} \leqslant 1$:

$$\theta_{n+1}^{(i)} = \frac{1}{1+\zeta^{(i)}\Delta p_{n+1}^{(i)}} \tag{31}$$

where $\Delta p_{n+1}^{(i)}$ can be obtained from Eqs. (26) and (27)

$$\text{For Model(I)}: \quad \Delta p_{n+1}^{(i)} = H(f_{n+1}^{(i)})\left\langle \Delta\boldsymbol{\varepsilon}_{n+1}^{\text{p}} : \frac{\boldsymbol{\alpha}_{n+1}^{(i)}}{\overline{\boldsymbol{\alpha}}_{n+1}^{(i)}} \right\rangle$$

$$f_{n+1}^{(i)} = \overline{\boldsymbol{\alpha}}_{n+1}^{(i)} - r^{(i)^2} \tag{32}$$

$$\text{For Model(II)}: \quad \Delta p_{n+1}^{(i)} = \left(\frac{\overline{\boldsymbol{\alpha}}_{n+1}^{(i)}}{r^{(i)}}\right)^{m^{(i)}} \left\langle \Delta\boldsymbol{\varepsilon}_{n+1}^{\text{p}} : \frac{\boldsymbol{\alpha}_{n+1}^{(i)}}{\overline{\boldsymbol{\alpha}}_{n+1}^{(i)}} \right\rangle \tag{33}$$

Thus, with the combination of Eqs. (20), (25) and (30),

$$\mathbf{s}_{n+1} - \boldsymbol{\alpha}_{n+1} = \mathbf{s}_{n+1}^{\text{trail}} - 2G\Delta\boldsymbol{\varepsilon}_{n+1}^{\text{p}} - \sum_{i=1}^{M}\theta_{n+1}^{(i)}\left(\boldsymbol{\alpha}_{n}^{(i)} + \frac{2}{3}h^{(i)}\Delta\boldsymbol{\varepsilon}_{n+1}^{\text{p}}\right) \tag{34}$$

Substitution of Eq. (19) into Eq. (34),

$$\mathbf{s}_{n+1} - \boldsymbol{\alpha}_{n+1} = \frac{\sigma_y\left(\mathbf{s}_{n+1}^{\text{trail}} - \sum_{i=1}^{M}\theta_{n+1}^{(i)}\boldsymbol{\alpha}_{n}^{(i)}\right)}{\sigma_y + 3G\Delta p_{n+1} + \sum_{i=1}^{M}\theta_{n+1}^{(i)}h^{(i)}\Delta p_{n+1}} \tag{35}$$

Replacement of Eq. (21) into the above condition gives

$$\Delta p_{n+1} = \frac{\left[\frac{3}{2}\left(\mathbf{s}_{n+1}^{\text{trail}} - \sum_{i=1}^{M}\theta_{n+1}^{(i)}\boldsymbol{\alpha}_n^{(i)}\right) : \left(\mathbf{s}_{n+1}^{\text{trail}} - \sum_{i=1}^{M}\theta_{n+1}^{(i)}\boldsymbol{\alpha}_n^{(i)}\right)\right]^{1/2} - \sigma_y}{3G + \sum_{i=1}^{M}\theta_{n+1}^{(i)}h^{(i)}} \tag{36}$$

The above non-linear algebraic equation which determines the value of accumulated plastic strain can be used further to calculate all internal variables corresponding to the end of increment $n+1$. The following steps are the details of algorithm for solving the problem:

Step 1. Update total strain value with a given strain increment $\Delta\boldsymbol{\varepsilon}_{n+1}$.
Setp 2. By computing the stress tensor at the elastic predictor phase, one obtains the so-called trial elastic stress. Check the yield condition from Eq. (7). If $F<0$, go back to step 1, or else $F>0$, then go to step 3.
Step 3. Suppose $\theta_{n+1}^{(i)}=1$ and calculate Δp_{n+1} by Eq. (36), and then update $\mathbf{s}_{n+1}-\boldsymbol{\alpha}_{n+1}$ by Eq. (35), $\mathbf{N}_{n+1}$ by Eq. (18), $\Delta\boldsymbol{\varepsilon}_{n+1}^{\text{p}}$ by Eq. (17), $\boldsymbol{\alpha}_{n+1}^{(i)}$ by Eq. (30), $\overline{\boldsymbol{\alpha}}_{n+1}^{(i)}(\overline{\boldsymbol{\alpha}}_{n+1}^{(i)}=\sqrt{3/2\boldsymbol{\alpha}_{n+1}^{(i)}:\boldsymbol{\alpha}_{n+1}^{(i)}})$, $\boldsymbol{\alpha}_{n+1}$ by Eq. (20), $\Delta p_{n+1}^{(i)}$ by Eqs. (32) and (33), and $\theta_{n+1}^{(i)}$ by Eq. (31).
Step 4. With the results of step 3, a new value of $\Delta p'_{n+1}$ is obtained with an update $\theta_{n+1}^{(i)}$. Compare the difference of $\Delta p'_{n+1}$ and Δp_{n+1} with a suitable tolerance. The iterations will be terminated when the tolerance of Δp_{n+1} can be satisfied, and the value under that condition will be adopted as the result at $n+1$.
Step 5. Examine whether the assigned total strain range has been reached. If not, go back to step 1, otherwise go to next step.
Step 6. Terminate the program here.

We will not discuss the accuracy and stability of backward Euler scheme, if the readers are interested in it, please refer to (Ortiz and Popov, 1985; Simo and Taylor, 1985, 1986; Kobayashi and Ohno, 2002) for more information.

5. Damage model

A typical damage evolution law proposed by Stolkarts et al., 1999 is adopted in this paper. Based on effective stress theory, one can use the effective compliance, $\overline{S}_{ijkl}$, which is the sum of an elastic compliance tensor of undamaged material S_{ijkl} and microcrack compliance tensor S^*_{ijkl}, to represent the effective stress tensor of the damaged material as below,

$$\bar{\sigma}_{kl} = \overline{S}^{-1}_{ijkl}S_{ijmn}\sigma_{mn} \tag{37}$$

A damage variable, D, representing a reduction in stiffness of the representative volume element, can be used to relate the elastic and shear modulus of undamaged material with the effective ones, given as:

$$\bar{\sigma} = \sigma(1-D) = \sigma\frac{\overline{E}}{E} \quad \text{uniaxial loading} \tag{38}$$

$$\bar{\tau} = \tau(1-D) = \tau\frac{\bar{\mu}}{\mu} \quad \text{pure shear loading} \tag{39}$$

It follows from this definition that $0 \leqslant D \leqslant 1$, where $D=0$ corresponds to undamaged material and $D=1$ to complete fracture of the representative volume element.

The expressions of effective elastic and shear modulus as functions of microcrack density, ω, for bodies containing random distribution of flat circular cracks, were derived by Budiansky and O'Connell (1976) and used here as follows:

$$\overline{E} = E\left[1 - \frac{16(1-(\bar{\nu})^2)(10-3\bar{\nu})}{45(2-\bar{\nu})}\omega\right] \tag{40}$$

$$\bar{\mu} = \mu\left[1 - \frac{32(1-\bar{\nu})(5-\bar{\nu})}{45(2-\bar{\nu})}\omega\right] \tag{41}$$

where the effective Poisson's ratio, $\bar{v}$, can be found from

$$\omega = \frac{45(v-\bar{v})(2-\bar{v})}{16(1-(\bar{v})^2)(10v-\bar{v}(1+3v))} \tag{42}$$

Its approximate value (if $v = 0.37$) can be obtained from $\bar{v} \sim \omega$ curve by least square fitting as:

$$\bar{v} = -0.579\omega + 0.37 \tag{43}$$

As it was pointed out by Stolkarts et al. (1999), the number of cycles to failure in the nucleation governed damage process was determined by

$$N_f = \frac{\bar{\omega}_c}{(\Delta\gamma^{cycle})^{\chi}} \tag{44}$$

$$\bar{\omega}_c = 0.093 + \eta\lambda_1^{-1.14} \tag{45}$$

where λ_1 was the non-dimensional specimen length, e.g., number of grains along characteristic length, and η was a constant. The critical microcrack density, $\bar{\omega}_c$, can be taken as 0.093 for a relatively large specimens corresponding to its larger characteristic length. $\Delta\gamma_i^{cycle}$ was an average shear strain range at a slip plane along a grain or phase boundary per cycle and χ was a material constant. It was assumed that the microcrack density ω increases at a constant rate during steady state of damage process, and the critical value will be reached until the final cycle occurs, i.e.,

$$\sum_{i=1}^{N_f} \Delta\omega_i^{cycle} = \bar{\omega}_c \tag{46}$$

$$\text{or } \Delta\omega_i^{cycle} = (\Delta\gamma^{cycle})^{\chi} \tag{47}$$

Since ω increases at a constant rate during steady state of damage process, the expression of Eq. (47) can be written as:

$$\omega = (\Delta\gamma^{cycle})^{\chi} N \tag{48}$$

where N is the number of cycles. Stolkarts et al. (1999) arbitrarily correlate $\Delta\gamma^{cycle}$ to the total strain range used in uniaxial fatigue test.

The life prediction technology in the multiaxial low cycle fatigue regime has made a great advance in recent decades (Brown and Miller, 1973; Kandil et al., 1982; Socie, 1987; Fatemi and Socie, 1988; Chen et al., 1999). Cracks tend to initiate on the maximum shear strain plane for the majority of metals in application, The initiated cracks usually propagate on the same plane (stage I) to a limited extent which varies with material and loading condition, and eventually the direction of propagation changes normal to the maximum stress (stage II) before the onset of unstable fracture. The crack initiation and stage I growth takes up much of the fatigue life and stage II growth is rather fast in most situations. Based on this mechanistic observation, a number of multiaxial fatigue parameters have been proposed in terms of shear and normal quantities on the maximum shear strain (or stress) plane, which is referred to as "critical plane approaches". The reasoning behind including normal strain or stress in the parameter is that it assists stage I crack growth, and thus plays a significant role on fatigue life.

Based on the experimental observations, the sum of maximum shear strain range and normal strain range on the critical plane, KBM parameter, (Kandil et al., 1982) is the best candidate to replace the uniaxial strain range for mix-mode loading conditions. Thus for a shear-type failure material, the normal strain will assist microcrack growth based on critical plane concept, Eq. (47) will be changed into:

$$\Delta\omega_i^{cycle} = (\Delta\gamma_i^{cycle})^{\chi} = k^{\chi}[\Delta\gamma_{max} + S\Delta\varepsilon_n]^{\chi} \tag{49}$$

where k is the proportionality constant, $\Delta\gamma_{max}$ is maximum shear strain range, $\Delta\varepsilon_n$ is normal strain range on the maximum shear strain critical plane. $S = 0.5$ is a material constant and can be determined by the experiments. With the substitution of Eq. (49) to Eq. (44), one has

Table 4
Parameters for Stolkarts's model based on Eq. (50)

Parameter	χ	k	$\bar{\omega}_c$
Value	1.78	0.187	0.093

$$N_f = \frac{\bar{\omega}_c}{k^{\chi}[\Delta\gamma_{max} + S\Delta\varepsilon_n]^{\chi}} \tag{50}$$

By fitting the above equation to the experimental data, the parameters can be obtained and listed in Table 4. Making an assumption that an elastic strain at peak stress was not affected by the damage, we can use expression (38) together with (40), (48) and (49) to establish the relation between effective equivalent stress and cycle number N

$$\bar{\sigma} = \left\{1 - \frac{16(1-(\bar{v})^2)(10-3\bar{v})}{45(2-\bar{v})} k^{\chi}[\Delta\gamma_{max} + S\Delta\varepsilon_n]^{\chi} N\right\}\sigma \tag{51}$$

With the combination of constitutive model in Section 3 and the damage model presented here, a particular damage coupled constitutive model can be obtained and used to compute the stress–strain hysteresis loops. The description of this process is following the same procedure as Stolkarts et al. (1998) did, and the flowchart was given as Fig. 2 in their paper, although the constitutive model is different.

6. Results and discussions

Ohno–Wang model was implemented to simulate the stress strain response of tin–lead solder over a wide range of loading conditions, as shown in Figs. 2 and 3. As seen from the figures, the Ohno–Wang model describes accurately the experiments under both uniaxial and torsional loadings. Since the predictions of Ohno–Wang model are not sensitive to the number of back stress components, and a rather rough approximation of monotonic tensile stress strain curves, which used to determine the parameters, still enables this model to give good estimations (Ohno, 1998), it is desirable to apply Ohno–Wang model to represent the inelastic deformation behavior of solder subjected to mix-mode loading conditions. Furthermore, the dependence of temperature and strain rate effect can be incorporated into Ohno–Wang model, and the implicit integration method can also be employed to solve these coupled equations (Kobayashi et al., 2003).

The damage evolution law adopted here was deduced from Stolkarts et al. (1999). Since tin–lead solder alloy belongs to shear-type failure material, the damage parameter used here is the sum of maximum shear strain range and normal strain on the critical plane to replace the uniaxial strain range used by Stolkarts. It is interesting to find that fatigue life of solder has a power law correlation with the equivalent strain range, which has a similar expression as a Coffin–Manson type equation, and the strain exponent in Eq. (50) is equal to 1.78 determined from our experimental observations. The strain exponent determined here is close to the typical value in Coffin–Manson equations reported for solders. The most attraction of the model what distinguishes it from traditional empirical equations is that it can accounts for the size effect in Eq. (45), which is substantial importance in microelectronics applications. Fig. 4 plots the relation of equivalent stress amplitude versus the number of cycles for all strain ranges under uniaxial and torsional loading, a similar description for two directions is found without exception. A typical curve showing the evolution of peak stress with cycles for 63Sn37Pb has three distinct regions representing different stages of fatigue, and the initial sharp drop in peak stress disappears as for small strain range of 0.2% under uniaxial loading and 0.346% under shear loading, respectively. One thing has to be noted that such transient stage of solder fatigue will also vanish when the equivalent strain range is greater than 1.5% with our limited experimental observations, more tests of large strain range are necessary to validate the conclusion. Comparing the experimental stress of first cycles with initial stress used for damage calculation, a relative large deviation due to the effect of stress sharp drop is occurred. Thus the transient stage cannot be ignored for large strain range when we coupled the damage evolution with constitutive model. Within the scope of our research, the material will reach the steady stage approximately after one fifth of its fatigue life, and the quantity of stress amplitude drop in first phase is highly

dependent on the applied strain range. The empirical relation below is used to correlate the damage value with strain amplitude at the end of transient stage:

$$D' = a \cdot \Delta\varepsilon_{eq} + b \quad \text{if } N = 1/5N_f \tag{52}$$

where D' is the damage value at the end of transient stage, $\Delta\varepsilon_{eq}$ is equivalent strain range, a and b are constants. When the number of cycles N exceeds one-fifth of fatigue life predicted by Eq. (50), the previous damage evolution equation will take effect, and the stress at that time can be calculated from D'. With this simple equation, the damage model can be incorporated into Ohno–Wang constitutive model to depict the stress strain response of different cycles with damage evolution, as can be seen in Figs. 2 and 3. By fitting it to the experimental data, a and b are determined as 22.3 and -0.029, respectively.

Fig. 5 plots the equivalent stress amplitudes together for uniaxial and torsional fatigue with the same equivalent strain amplitudes, it indicates that shear stress in torsion decays more rapidly than the axial stress in uniaxial fatigue. One assumes the isotropic characteristics of this material and a scalar damage variable relative to

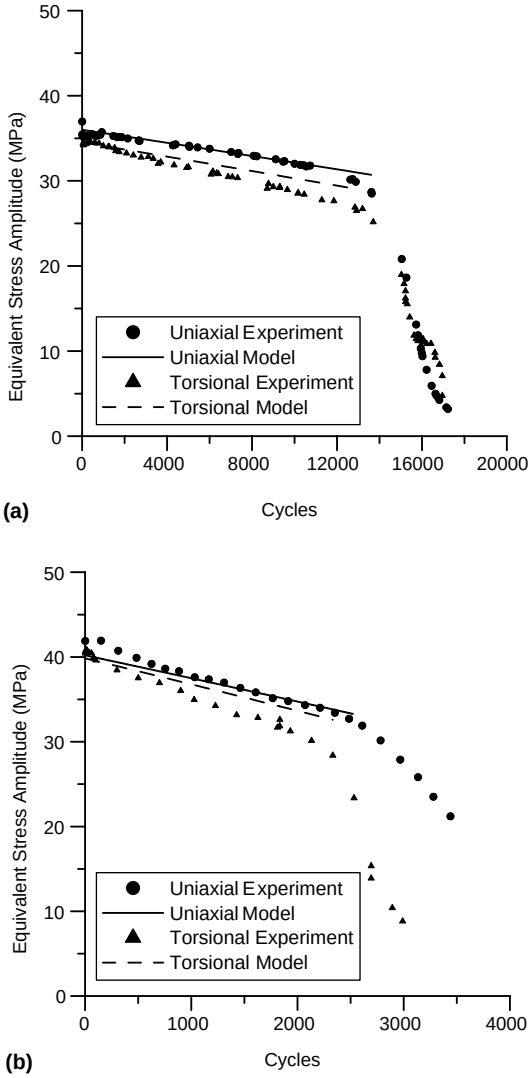

Fig. 5. Comparison of the equivalent stress amplitude evolution with the number of cycles for uniaxial and torsional fatigue: (a) $\Delta\varepsilon_{eq}/2 = 0.2\%$ and (b) $\Delta\varepsilon_{eq}/2 = 0.5\%$.

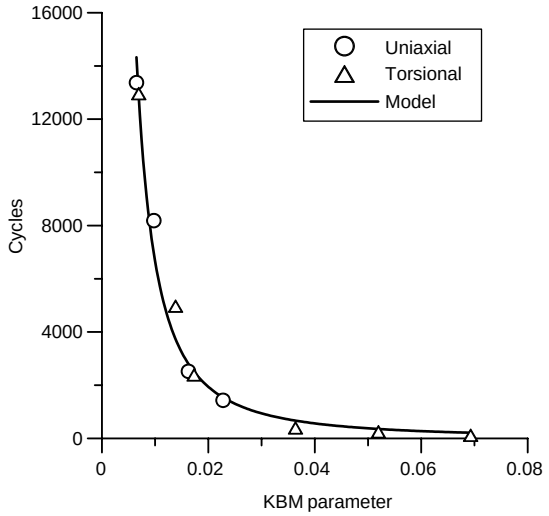

Fig. 6. KBM parameter versus fatigue life.

effective elastic moduli employed here to represent the damage evolution. As shown in Fig. 5, the simulations of peak stress decline with isotropic assumption correlate the experiment fairly well.

The coupling of damage and constitutive model is used to predict the stress strain behavior of solder under uniaxial and torsional loading, and the results are given in Figs. 2 and 3. With the consideration of Eq. (52), the complex inelastic and damage behavior of solder can be reproduced accurately by the model. Further research is necessary to establish a correlation base upon micromechanics to describe the first stage of stress drop instead of this empirical approach, and the coupled model need to be implemented into finite element analysis in order to describe the response of actual packaging structure under thermal fatigue loading.

The high efficiency and excellent accuracy of backward Euler integration method make the program save lots of calculating time and make it desirable to be used for cyclic loading conditions. As we know that the computational time depends not only on the capability of computer, but also on the tolerance and the number of equilibrium points for each cyclic loading. For example, on a standard personal computer with 500 MHz CPU and 192 MB SDRAM, when the tolerance equals to 10^{-5} and 32 equilibrium points are set for each cycle, the computational time required to complete the simulation of 10 000 cycles is approximately 10 h.

Experimental data obtained from uniaxial and torsional loading test and the curve generated by Eq. (50) are plotted on Fig. 6, where the coefficient of determination R-squared is 0.982. The perfect correlation between experiment and model verifies the validity of fatigue life prediction model. Actually, the solder life obtained by this approach is ≈60–80% of its total life because the failure criterion defined here seems somewhat conservative. However, the lifetime estimation determined by this criterion is important since it can be used to judge the end of the second stage in the damage evolution curve of solder, and it is a not bad choice for failure definition in a safe design practice.

7. Conclusion

A series of fatigue tests under uniaxial and torsional loading at constant room temperature is carried out. A cyclic constitutive and damage model is presented in this paper to describe the characterization of stress strain response and damage evolution for these fully reversed strain controlled tests. The following conclusions are obtained:

1. Ohno–Wang model is quite suitable to simulate the cyclic plastic deformation of tin–lead material over a wide range of uniaxial and trosinoal loading conditions at room temperature. The application of backward Euler method improves efficiency and save computing time without losing accuracy.

2. Comparing the peak stress decline curve between shear and axial direction with the same equivalent strain amplitude, it can be found that the shear stress in torsion decays more rapidly than the axial stress, this is because tin–lead solder belongs to shear-type failure material. Base on the experimental observations, it is reasonable to assume that isotropic characteristics of this material and a scalar damage variable relative to effective elastic modulus employed to represent the damage evolution. With the combination of critical plane approach, the phenomena can be predicted fairly well.
3. It is found that KBM parameter, the sum of maximum shear strain range and normal strain amplitude on maximum shear plane, is a good candidate for replacing uniaxial strain range originally used in Stolkarts's model. The parameter can be applied to multiaxial fatigue further. In addition, the fatigue life prediction model can account for the size effect, which is substantial importance in microelectronics applications.
4. With the consideration of stress sharp drop stage, the coupling damage and Ohno–Wang constitutive model of 63Sn37Pb is easy to be applicable and predicts the complex inelastic deformation of solder reasonably accurately. It is also possible to take into account the influence of temperature and strain-rate dependence on stress–strain response by extending the present work. Further research is necessary to incorporate these characteristics of the model together, and the corresponding experiments are required to verify them.

Acknowledgement

The authors gratefully acknowledge financial support for this work from National Natural Science Foundation of China (No. 10272080), NSFC Oversea Outstanding Young Scholar Project, and the Teaching and Research Award Program for Outstanding Young Teachers in Higher Education Institutions of MOE, PR China.

References

Basaran, C., Chandaroy, R., 1998. Mechanics of Pb40/Sn60 near-eutectic solder alloys subjected to vibrations. Appl. Math. Modell. 22, 601–627.

Basaran, C., Yan, C., 1998. A thermodynamic framework for damage mechanics of solder joints. ASME J. Electron. Packag. 120, 379–384.

Brown, M.W., Miller, K.J., 1973. A theory for fatigue failure under multi-axial stress–strain conditions. Proc. Inst. Mech. Eng. 187 (65), 745–755.

Brown, M.W., 1978. Torsional stresses in tubular specimens. J. Strain Analysis 13, 23–28.

Budiansky, B., O'Connell, R.J., 1976. Elastic moduli of a cracked solid. Int. J. Solids Struct. 12, 81–97.

Chaboche, J.L., 1998a. Continuum damage mechanics: Part I—General concepts. ASME J. Appl. Mech. 55, 59–64.

Chaboche, J.L., 1998b. Continuum damage mechanics: Part II—Damage growth, crack initiation, and crack growth. ASME J. Appl. Mech. 55, 65–72.

Chen, X., Chen, G., Sakane, M., 2005. Prediction of stress–strain relationship with an improved Anand constitutive model for lead free solder Sn–3.5Ag. IEEE Trans. Comp. Manuf. Packag. Tech. 28, 111–116.

Chen, X., Song, J., Kim, K.S., Fatigue life of 63Sn–37Pb solder related to loading drop under uniaxial and torsional loading. Int. J. Fatigue, in press.

Chen, X., Song, J., Kim, K.S., Low cycle fatigue life prediction of 63Sn-37Pb solder under proportional and non-proportional loading. Int. J. Fatigue, in press.

Chen, X., Xu, S., Huang, D., 1999. A critical plane-strain energy density criterion for multiaxial low-cycle fatigue life under non-proportional loading. Fatigue Fract. Eng. Mater. Struct. 22, 679–686.

Darveaux, R., 2002. Effect of simulation methodology on solder joint crack growth correlation and fatigue life prediction. ASME J. Electron. Packag. 124, 147–154.

Duxbury, P., Crook, T., Lyons, P., 1994. A consistent formulation for the integration of combined plasticity and creep. Int. J. Numer. Meth. Eng. 37, 1277–1295.

Fatemi, A., Socie, D.F., 1988. A critical plane approach to multiaxial fatigue damage including out-of-phase loading. Fatigue Fract. Eng. Mater. Struct. 11, 149–165.

Fine, M.E., Stolkarts, V., Keer, L.M., 1999. Fatigue crack nucleation assisted by thermal activation. Mater. Sci. Eng. A272, 5–9.

Fu, C., McDowell, D., Ume, C., 1996. Time integration procedures for a cyclic thermoviscoplasticity model for Pb–Sn solder applications. In: IEEE Proceedings of Electronic Components and Technology Conference, pp. 403–413.

Hartmann, S., Lührs, G., Haupt, G., 1997. An efficient stress algorithm with applications in viscoplasticity and plasticity. Int. J. Numer. Meth. Eng. 40, 991–1013.

Jiang, Y.Y., Kurath, P., 1996. Characteristics of the Armstrong–Frederick type plasticity models. Int. J. Plast. 12, 387–415.
Kandil, F.A., Brown, M.W., Miller, K.J., 1982. Biaxial Low-cycle Fatigue Fracture of 316 Stainless Steel at Elevated Temperatures. Book 280. The Metals Society, London, pp. 203–210.
Kobayashi, M., Ohno, N., 2002. Implementation of cyclic plasticity models based on a general form of kinematic hardening. Int. J. Numer. Meth. Eng. 53, 2217–2238.
Kobayashi, M., Mukai, M., Takahashi, H., Ohno, N., Kawakami, T., Ishikawa, T., 2003. Implicit integration and consistent tangent modulus of a time-dependent non-unified constitutive model. Int. J. Numer. Meth. Eng. 58, 1523–1543.
Lim, T.J., Lu, W.Y., 2001. Multi-axial cyclic and monotonic behavior of a 63Sn–37Pb solder alloy. In: ASME International Mechanical Engineering Congress and Exposition, American Society of Mechanical Engineers, EEP, vol. 1, pp. 231–236.
Lin, H., Nayeb-Hashemi, H., Pelloux, R.M.N., Berg, C.A., 1992. Cyclic deformation and anisotropic constitutive relations of Al-6061-T6 under biaxial loading. ASME J. Eng. Mater. Tech. 114, 323–330.
Low, S.R., Fields, R.J., Lucey, G.K., 1991. Multiaxial mechanical behavior of 63Sn–37Pb Solder. In: IEEE Proceedings of Electronic Components and Technology Conference, pp. 292–298.
Lush, A.M., Weber, G., Anand, L., 1989. An implicit time-integration procedure for a set of internal variable constitutive equations for isotropic elasto-viscoplasticity. Int. J. Plast. 5, 521–549.
Marin, E.B., McDowell, D.L., 1997. A semi-implicit integration scheme for rate-dependent and rate-independent plasticity. Comput. Struct. 63 (3), 579–600.
Miller, K.J., Chandler, D.C., 1970. High strain torsion fatigue of solid and tubular specimens. Proc. Inst. Mech. Eng. 2 (4), 262–270.
Ohno, N., 1998. Constitutive modeling of cyclic plasticity with emphasis on ratchetting. Int. J. Mech. Sci. 40, 251–261.
Ohno, N., Wang, J.D., 1993a. Kinematic hardening rules with critical state of dynamic recovery, part I: formulations and basic features for ratcheting behavior. Int. J. Plast. 9, 375–390.
Ohno, N., Wang, J.D., 1993b. Kinematic hardening rules with critical state of dynamic recovery, Part II: application to experiments of ratchetting behavior. Int. J. Plast. 9, 391–403.
Ortiz, M., Popov, E.P., 1985. Accuracy and stability of integration algorithms for elastoplastic constitutive relations. Int. J. Numer. Meth. Eng. 21, 1561–1576.
Ortiz, M., Simo, J.C., 1986. An analysis of a new class of integration of integration algorithms for elastoplastic constitutive relations. Int. J. Numer. Meth. Eng. 23, 353–366.
Schroeder, S.A., Mitchell, M.R., 1992. Torsional creep behavior of 63Sn–37Pb solder. In: Proceedings of the 1992 Joint ASME/JSME Conference on Electronic Packaging Part 2, pp. 649–653.
Smith, J.F., Kubalak, R.R., 1979. Tin and tin alloy, ninth ed.Metals Handbook, 2 American Society for Metals, Metals Park (OH), pp. 613–625.
Stolkarts, V., Moran, B., Keer, L.M., 1998. Constitutive and damage model for solders. In: IEEE Proceedings of Electronic Components and Technology Conference, pp. 379–385.
Stolkarts, V., Keer, L.M., Fine, M.E., 1999. Damage evolution governed by microcrack nucleation with application to the fatigue of 63Sn–37Pb solder. J. Mech. Phys. Solids 47, 2451–2468.
Stolkarts, V., Keer, L.M., Fine, M.E., 2001. Constitutive and cyclic damage model of 63Sn–37Pb solder. ASME J. Electron. Packag. 123, 351–355.
Simo, J.C., Taylor, R.L., 1985. Consistent tangent operators for rate-independent elastoplasticity. Comp. Meth. Appl. Mech. Eng. 48, 101–118.
Simo, J.C., Taylor, R.L., 1986. A return mapping algorithm for plane stress elastoplasticity. Int. J. Numer. Methods Eng. 22, 649–670.
Socie, D.F., 1987. Multiaxial fatigue damage models. ASME J. Eng. Mater. Tech. 109, 293–298.
Tang, H., Basaran, C., 2003. A damage mechanics-based fatigue life prediction model for solder joints. ASME J. Electron. Packag. 125, 120–125.
Vaynman, S., Fine, M.E., Jeannotte, D.A., 1990. Low-cycle isothermal fatigue life of solder materials. Solder Mechanics—A State of the Art Assessment. TMS, Pennsylvania, USA, pp. 155–189.
Wei, Y., Chow, C.L., Fang, H.E., Neilsen, M.K., Lim, T.J., Lu, W., 2004. Failure analysis of miniature solder specimen. ASME J. Electron. Packag. 126, 100–105.
Yang, X.J., Chow, C.L., Lau, K.J., 2004. Time integration algorithm for a cyclic damage coupled thermo-viscoplasticity model for 63Sn–37Pb solder applications. ASME J. Electron. Packag. 126, 148–158.